Journal of Ocean Engineering and Marine Energy
https://doi.org/10.1007/s40722-019-00129-8

SAND2019-4731J

RESEARCH ARTICLE

CFD design-load analysis of a two-body wave energy converter

Ryan G. Coe[1] · Brian J. Rosenberg[3] · Eliot W. Quon[2] · Chris C. Chartrand[1] · Yi-Hsiang Yu[2] · Jennifer van Rij[2] · Tim R. Mundon[3]

Received: 15 September 2018 / Accepted: 22 January 2019

Abstract
Wave energy converters (WECs) must survive in a wide variety of conditions while minimizing structural costs, so as to deliver power at cost-competitive rates. Although engineering design and analysis tools used for other ocean systems, such as offshore structures and ships, can be applied, the unique nature and limited historical experience of WEC design necessitates assessment of the effectiveness of these methods for this specific application. This paper details a study to predict extreme loading in a two-body WEC using a combination of mid-fidelity and high-fidelity numerical modeling tools. Here, the mid-fidelity approach is a time-domain model based on linearized potential flow hydrodynamics and the high-fidelity modeling tool is an unsteady Reynolds-averaged Navier–Stokes model. In both models, the dynamics of the WEC power take-off and mooring system have been included. For the high-fidelity model, two design wave approaches (an equivalent regular wave and a focused wave) are used to estimate the worst case wave forcing within a realistic irregular sea state.These simplified design wave approaches aim to capture the extreme response of the WEC within a feasible amount of computational effort. When compared to the mid-fidelity model results in a long-duration irregular sea, the short-duration design waves simulated in CFD produce upper percentile load responses, hinting at the suitability of these two approaches.

Keywords Wave energy converter (WEC) · Extreme · Survival · Design load · CFD

1 Introduction

A wide variety of methods and models are utilized in the design of wave energy converters (WECs). An excellent survey of current practices utilized by WEC developers, along with a design-load case study, is provided by Arup and Atcheson (2016). A generalized survey of WEC design practices, considering environmental characterization, modeling, experimental analysis, fatigue, and extreme value analysis, was performed by Coe et al. (2018b). Currently, the only formal guidance for the design-load analysis of WECs is given in IEC TS 62600-2 (2016).[1] This Technical Specification (TS) combines a finite set of operational and extreme environmental conditions to be combined with transportation, assembly, production, and parked/survival device states to define design-load cases that should be analyzed to predict ultimate and fatigue loading of a WEC. Additionally, informal guidance can be garnered from related standards and guidance documents, including those focused on offshore wind (IEC TS 61400-3-2 2013 and DNV-OS-J103 2013) and offshore oil and gas structures (DNV-RP-F205 2010).

In IEC TS 62600-2, the environmental conditions for design cases are generally defined as the conditions that provide the largest response (e.g., the sea state along the 50-year contour that elicits the largest load). This presents a challenging problem when it comes time to predict these loads via modeling or experiments, as the designer must balance accuracy of the prediction with efficiency of the model or experiment. To accurately model a realistic sea state, experiments (both numerical and physical) need to evaluate irregular seas until statistical convergence is observed—typically 3 h (e.g., Ochi 2005). For performance (i.e., energy production) evaluation, linear and lower order models, such as those based on the hydrodynamics from a boundary element model (BEM), are heavily utilized. However, it is well known that

✉ Ryan G. Coe
rcoe@sandia.gov

[1] Sandia National Labs, Albuquerque, NM, USA

[2] National Renewable Energy Laboratory, Golden, CO, USA

[3] Oscilla Power, Inc., Seattle, WA, USA

[1] Following the first release of IEC TS 62600-2 in 2016, a revision of IEC TS 62600-2 is currently under development.

Published online: 02 April 2019

the linear assumptions of such models break down in large waves and that these lower order models may, therefore, lose accuracy. Thus, a more appropriate numerical model formulation, such as those offered by computational fluid dynamics (CFD) models based on the Navier–Stokes equations, is often considered for the prediction of extreme design loads for WECs. However, along with the high computational cost of the higher fidelity models comes the need for methods or procedures for practical application of these models.

For other ocean engineering systems, best practices have been established by designers to determine when higher fidelity models are necessary. While these best practices may not also be completely prescriptive, they provide useful guidelines when analyzing, e.g., a new semi-submersible structure with many comparable predecessors. WECs have a much shorter history of focused design and analysis. This means that the problem of selecting models and approaches to perform different steps in the design process is much less defined. There is thus a need for increased experience in the various WEC design stages, perhaps most dramatically in analyzing extreme conditions.

To balance the needs for accuracy with the cost of high-fidelity modeling, a multi-step process for assessing design loads, similar to that used by van Rij et al. (2018), has been applied in this study. Figure 1 shows a workflow diagram of this process as realized in this study. First, a series of simulations are run with a mid-fidelity model to predict the maximum response across the set of sea states currently being considered for the operation of the system in question. From the results of these mid-fidelity simulations, two design-load case sea states of interest are chosen ("SS01" and "SS02" in Fig. 1). For each sea state of interest, two types of design wave realizations are defined: an equivalent regular wave and a focused wave (design wave realizations are be discussed in further detail in Sect. 2.2). The device response to the resulting four design waves are then simulated using a CFD model of the system of interest.

This paper will first present a brief discussion of relevant considerations for the CFD model along with a review of previous work in this area. Next, we introduce the study device in further detail. The mid-fidelity modeling results will be summarized and the selection of two design-load cases will be made. A methods section will then discuss the configuration of the CFD model and the definition of the four design waves. Finally, results will be presented and discussed.

1.1 On modeling WECs in CFD

CFD models are seeing increasing usage for the analysis of WECs. However, while there has been extensive usage of CFD for analysis of ships and offshore structures, CFD analyses of WECs remain challenging and have thus had relatively little widespread inclusion in WEC design processes. Although many of the best practices for CFD analysis of ships and offshore structures (e.g., ITTC 2011) can be applied for WECs, WECs present some unique problems from a CFD-modeling standpoint. The most fundamental obstacle which must be addressed is the inclusion of multi-body dynamics with various linkages or joints and subsystem dynamics. To model such a system in CFD, two issues arise: (1) capturing moving bodies in the computational domain (i.e., mesh) and (2) solving the multibody dynamic problem to include PTOs and mooring system dynamics.

Item 1 can be addressed by mesh-based CFD models via mesh deformation ("morphing"), sliding interfaces, and overset (Chimera) meshes (see, e.g., Ferziger and Peric 2012; Hadzic et al. 2005, for excellent discussions on moving meshes). Note that in the case of a single-body device, it is also possible to simply allow the entire computational domain to move with the body (i.e., with a moving reference frame). Each of these approaches has its advantages and drawbacks. Mesh deformation or morphing cannot easily handle large-amplitude motions and is challenging to implement for systems where two separate bodies are located near to each other with close clearances. Sliding interfaces are

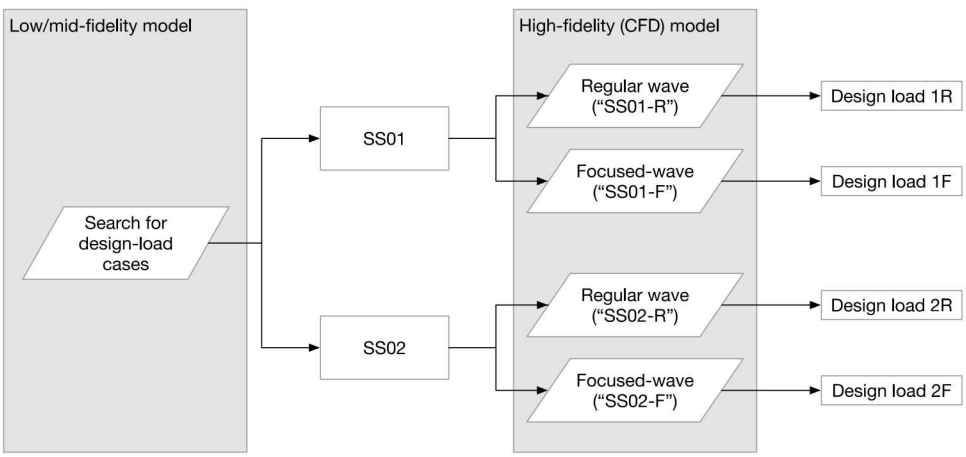

Fig. 1 Workflow for design-load analysis of the Triton WEC

quite efficient, but can only accommodate certain types of motion (e.g., a spinning rotor). Overset meshes are perhaps the most adaptable because, with appropriate meshing, they can handle large-amplitude motion and close clearances, but are not without their disadvantages. In particular, overset meshes can suffer from reflection and damping introduced by interpolation at the interface between a background and overset mesh.

Item 2 is often handled on an ad hoc basis. Some CFD software packages include functionality for prescribing joints between bodies. However, including additional dynamics, e.g, for a PTO force per some arbitrary control law, will require some custom coding. As the complexity of these additional dynamics systems increases, custom coding becomes impractical and gives way to a need to couple external models.

Meshless CFD methods, such as smoothed-particle hydrodynamics (SPH), are receiving increasing attention (e.g., Crespo et al. 2015; Hérault et al. 2010). While these methods remain somewhat less developed than "traditional" finite-volume CFD, meshless CFD methods have the potential to become quite useful for modeling WECs. First, as they inherently require no mesh, the above issues with various moving mesh solutions are removed. Second, many of the challenges of modeling a free surface, which requires specialized meshing and solver settings in finite-volume CFD simulations, are avoided. However, SPH implementations do not handle viscous effects and computation of the pressure field as easily as mesh-based CFD.

A number of studies have been conducted to utilize CFD in predicting WEC responses. To the authors' knowledge, the devices studied have comprised entirely of single-body devices, including fixed (Iturrioz et al. 2015), single degree of freedom (Penalba et al. 2018; Ransley et al. 2017b; Madhi and Yeung 2017; Westphalen et al. 2009; Hu et al. 2011), and tethered multiple degrees of freedom (Quon et al. 2016; Omidvar et al. 2013; Westphalen et al. 2014; Rafiee et al. 2016; Ransley et al. 2017a; Sjökvist and Göteman 2017; Palm et al. 2016) bodies or devices. (Additionally, Yu and Li (2013) studied a two-body WEC in which the relative motion between the two bodies was locked). These simulations have generally shown good agreement with experimental data when available. The analyses to date have utilized mainly finite-volume volume-of-fluid (VOF) CFD (Penalba et al. 2018; Quon et al. 2016; Yu and Li 2013; Westphalen et al. 2009; Ransley et al. 2017a, b; Rafiee et al. 2016; Palm et al. 2016; Iturrioz et al. 2015; Hu et al. 2011) and SPH (Madhi and Yeung 2017; Westphalen et al. 2014; Omidvar et al. 2013). These previous studies have used both regular waves (Ransley et al. 2017b; Madhi and Yeung 2017; Sjökvist and Göteman 2017; Palm et al. 2016; Yu and Li 2013) and focused waves (Sjökvist and Göteman 2017; Ransley et al. 2017a; Quon et al. 2016; Rafiee et al. 2016; Westphalen et al. 2014; Omidvar et al. 2013; Hu et al. 2011; Westphalen et al. 2009).

1.2 Study device

As a case study, the design-load methodology depicted in Fig. 1 is applied to the Triton WEC, a two-body quasi point absorber under development by Oscilla Power, Inc. (OPI). The Triton WEC is a 1 MW-rated utility-scale device intended for deployment in fully energetic ocean environments, such as the U.S. west coast. A diagram of the device in operational mode is shown in Fig. 2. The device is composed of two bodies—a 30-m-long surface float and a submerged reaction ring structure—that are coupled together by three flexible ropes ("tendons"). As the surface float is excited by the wave resource, the two bodies move and react relative to each other; the resulting tension variations in each tendon drive three separate power take-off (PTO) systems housed inside the surface float. Due to the three separate tendons and PTO systems, energy is captured from all degrees of relative motion in translation and rotation.

For each of the three tendons, the Triton PTO at the simplest level consists of two components: a "return spring" and a generator, described in further detail by Mundon et al. (2017a). The return spring is a hydropneumatic system that supports the mean underwater weight of the reaction ring, approximately 1,300 metric tons, and also provides a spring functionality to keep the mean PTO position at the center of travel. The associated spring rate is approximately linear and can be varied based on the sea state. The generator is a Vernier linear machine that converts captured mechanical energy into electricity. While the PTO is capable of implementing advanced control strategies, particularly to maximize power capture in smaller waves, this study will employ a simple proportional damping strategy due to the larger and extreme waves examined. Here, the hydropneumatic system and generator are approximated by a linear spring and damper, respectively, with the added constraints that the PTO must avoid end-stop impacts and the tendons must remain taut.

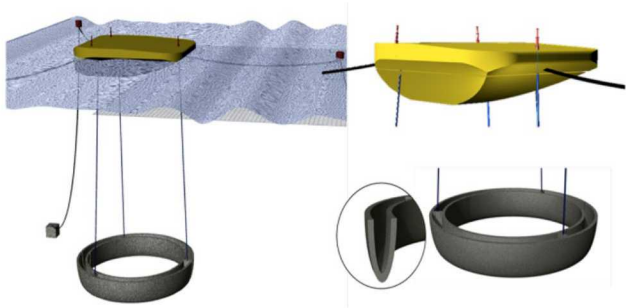

Fig. 2 Illustration of the Triton WEC

As shown in Fig. 2, the WEC is moored using a three-point inverted catenary arrangement. Each mooring leg comprises an upper line segment, attached to the surface float, and a lower line segment, anchored to the seafloor, with the two lines connected by an intermediate cylindrical line float. This arrangement provides a soft horizontal station-keeping force while exerting minimal vertical forces on the WEC.

In this study, we are interested in the maximum design loads for the tendons and moorings during a hypothetical Triton deployment off the coast of California (U.S. Department of Energy Humboldt Bay reference location). The design envelope was selected to be the 50-year wave contour, where significant wave heights (H_s) can reach up to approximately 10 m in extreme sea states (Dallman and Neary 2014). However, in sea states where H_s is larger than approximately 5 m, the WEC reconfigures from the "operational" configuration (Fig. 2) and enters a different "survival" configuration to improve device survivability at the expense of reduced power capture.

In this load-shedding configuration, tendon and mooring loads are greatly reduced; the resulting scenario is that the maximum tendon and mooring loads are driven by the largest waves in which the device is in the operational configuration. The maximum operational contour then becomes a design choice and is selected here to be in the vicinity of $H_s = 5$ m based on various system constraints, specifically the PTO travel, minimum allowable tendon tension, and rated electrical power of the generators. For the purposes of the current study, we will focus on these wave conditions where the device is in operational mode as these will drive the design for the tendons and the moorings.

2 Methods

2.1 Mid-fidelity numerical model

Further details and validation of the mid-fidelity model used in the current study have been presented by Rosenberg and Mundon (2016). The equations of motion for the coupled marine and PTO systems of the Triton WEC were solved in the time domain using the commercial marine dynamics software Orcina Orcaflex (2015). Linearized frequency response functions (FRFs) for the surface float added mass, radiation damping, and wave excitation were obtained from the BEM solver NEMOH (Babarit and Delhommeau 2015). Fluid memory effects for the surface float were implemented in OrcaFlex using the convolution integral method ("Cummins equation").

The reaction ring, which interacts minimally with the free surface, is modeled using a bulk Morison formulation in each degree of freedom. The hydrodynamic contributions to the reaction ring force, in the form of added mass and viscous drag, have undergone extensive study and characterization using CFD and laboratory experiments (Mundon et al. 2017b).

The Triton mooring arrangement described in Sect. 1.2 may be represented by an equivalent linear horizontal spring stiffness and pretension acting at the surface float center of gravity. This first-order mathematical approximation will be used for the CFD simulations presented in this study, whereas the full mooring line dynamics are solved using a finite element representation in the mid-fidelity OrcaFlex simulations.

To satisfy the "low-/mid-fidelity" simulations called for in Fig. 1, OrcaFlex simulations of the Triton device were run at a series of sea states along the maximum operational wave contour as discussed in Sect. 1.2. All sea states were represented by a Bretschneider wave spectrum, and the incident wave direction for all simulations was aligned with the primary wave direction of the Triton WEC (waves travel from right to left in Fig. 2). In accordance with DNV-GL guidelines, the duration of each simulation was 3 hours and the time step was $\Delta t = 0.005$ s. To achieve well-converged statistics, 6 independent realizations of each sea state were run, wherein each realization had a randomly generated phasing for the constitutive wave components.

From these simulations, two sea states of interest (SS01 and SS02 in Fig. 1) were selected for further investigation with CFD. These cases, and the corresponding maximum tendon and mooring tensions predicted by OrcaFlex for these sea states, are shown in Table 1. Note that the maximum responses are taken as the average of the maxima from each of the six sea state realizations. The case SS01 was chosen as it represents the critical loading case for the tendon tensions, which occurs in the forward tendon. Case SS02 is not the critical load case for the mooring tension (this occurs at even longer period waves), but was selected to provide an additional useful comparison point between the CFD and OrcaFlex predictions.

Table 1 Design-load cases of interest based on the mid-fidelity model

ID	Sig. wave height, H_s (m)	Peak period, T_p (s)	Peak wavelength, λ_p (m)	Peak phase speed, c_p (m/s)	Eq. reg. wave height, H_{reg}(m)	Max tendon load (MN)	Max mooring load (MN)
SS01	4.75	9.2	132	14.4	9.0	8.76	0.699
SS02	5.25	16.2	410	25.3	9.9	7.16	0.857

2.2 Design waves

Due to the impractically long computational times that would be required to obtain statistically converged device response in a realistic irregular sea state using CFD, two design wave approaches were selected: regular and focused waves (e.g., Coe et al. 2018b). Thus, from the two design cases selected in Sect. 2.1, we define a total of four sea states for evaluation (see Fig. 1). The two regular-wave cases are referred to as SS01-R and SS02-R, respectively. Likewise, the focused waves are referred to as SS01-F and SS02-F.

To produce the regular design waves, following common guidance found in N-0003 and DNV-RP-C205, we can substitute the irregular sea state with a regular wave, where $H_{\text{reg}} = 1.9H_s$ (NORSOK 2007; DNV-RP-C205 2007). Note it is generally recommended that multiple regular design waves, with a range of periods, be considered. However, lacking the resources to run many simulations of this type, the peak period of the irregular sea states was used here. Regular design waves are, in effect, a simplified representation of highly peaked, wind-generated, fetch-limited seas. In the limit, the energy bandwidth of the sea approaches zero and we are left with a regular wave. The factor 1.9 comes from the common assumption of the free-surface process to follow a Rayleigh distribution (e.g., Ochi 2005). Thus, Table 1 gives the equivalent regular-wave heights for SS01 and SS02.

Focused waves combine a set of individual frequency components at a specified point and time, resulting in a large single crest. Focused waves for this study were constructed using the most likely extreme response (MLER) method (Quon et al. 2016; Coe et al. 2018a). To develop the focused waves used in this study (SS01-F and SS02-F), OrcaFlex simulations were run with white-noise spectra with significant wave heights equivalent to those of SS01 and SS02 for 1 h each with a time step of $\Delta t = 0.01$ s. This approach gives better results than using idealized spectra (e.g., the exact Bretschneider spectra from SS01 and SS02) because the input energy (that contained in the waves) is more evenly spread across the frequencies of interest. Using white-noise waves is generally not feasible in wave tank testing because the waves tend to break, but the OrcaFlex model does not model breaking waves. This time history was used to estimate the wave and response spectra, from which the FRFs for the tendon and mooring line responses were determined. A Blackman window was found to be most effective for minimizing spectral leakage and preserving the peak spectral amplitude. In addition, uniform filtering of the calculated power spectral density was performed according to data processing techniques for similar offshore wave data. For both operations, the filtering window included 8 s of data.

The resulting FRFs for both cases are shown in Fig. 3a, b. The upper and lower plots in each figure show the response

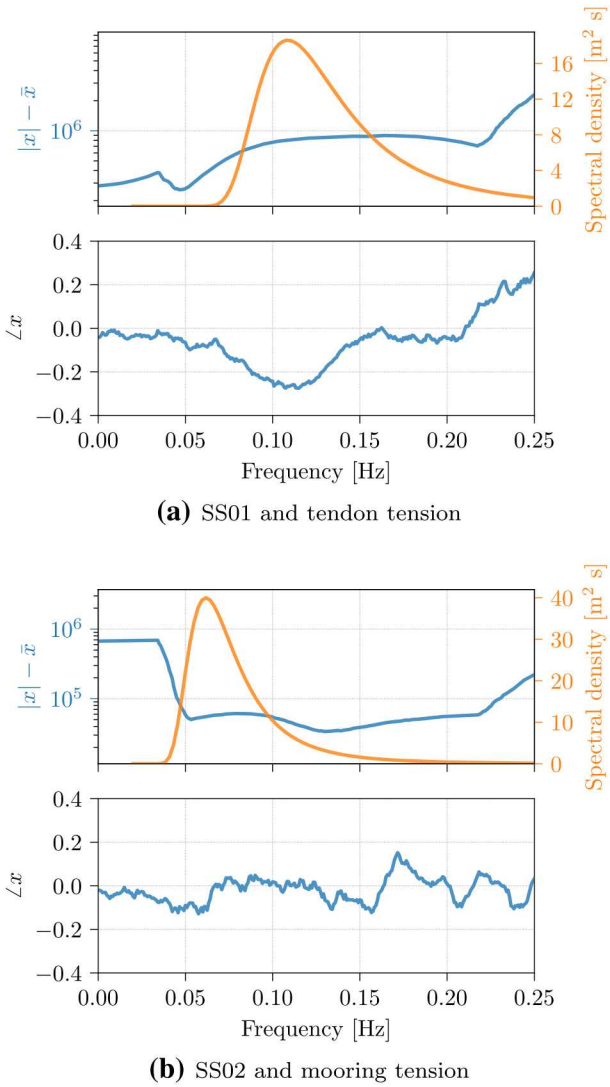

Fig. 3 Frequency response functions (blue) shown with wave spectra (orange) (color figure online)

magnitude and relative phase, respectively. The SS01 and SS02 spectra, which are in combination with the FRFs to create the focused waves, are overlaid on the FRFs in these figures. The low-frequency energy content observed in Fig. 3b is somewhat typical of the low-frequency dynamic behavior of mooring systems. Note that since the FRFs were created with band-limited input, the signal-to-noise-ratio decreases rapidly when $f < 0.05$ Hz. To prevent erroneous waves from being created in this region, no energy content is allowed in the input spectra for these frequency ranges.

The focused-wave elevation (at the device location) and response time histories were calculated as per Quon et al. (2016). For SS01-F, the tendon tension FRF was used. For SS02-F, the mooring tension FRF was used. The resulting focused waves and expected responses for the tendon and mooring tension are shown in Fig. 4a, b, respectively. These

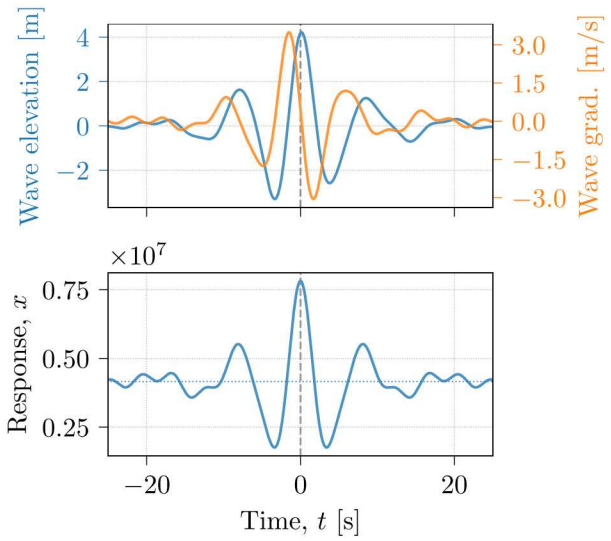

(a) SS01 and tendon tension

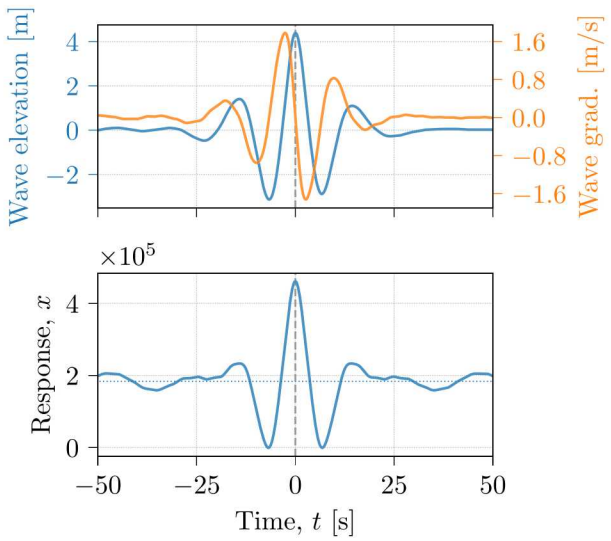

(b) SS02 and mooring tension

Fig. 4 SS01-F focused wave and expected response for tendon tension

focused design waves are simulated in the CFD model discussed in the subsequent sections. Note that Fig. 4 shows the predicted responses based on the MLER theory, with tendon and mooring tension maxima of 7.82 MN and 0.462 MN, respectively.

2.3 Computational fluid dynamics model

The commercial CFD code STAR-CCM+ was used to model the Triton device. Figure 5 shows an illustration of the Triton device as modeled in CFD. Only planar motion was

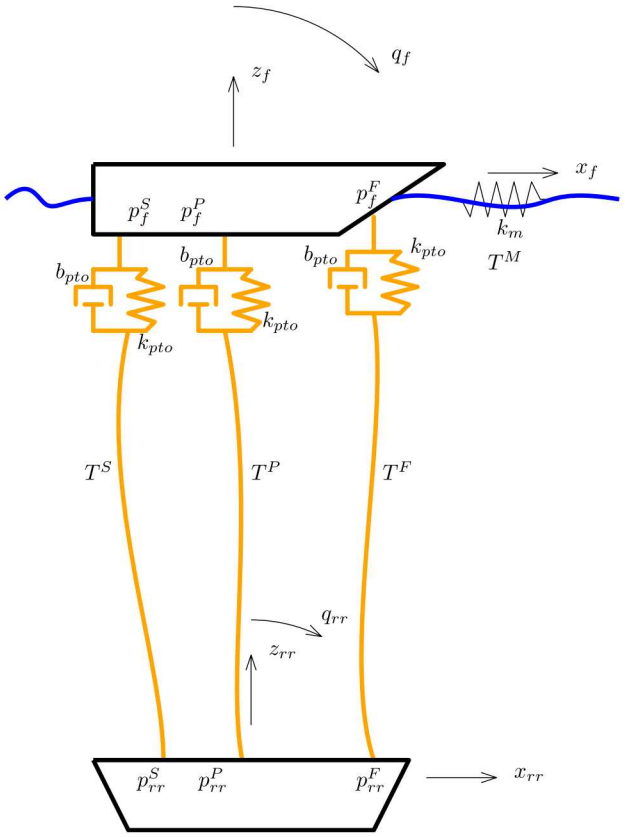

Fig. 5 Diagram of Triton device for simulation

considered in this study, thus both the float and reaction ring were allowed three degrees of freedom: heave (z), surge (x), and pitch (q). Unidirectional waves aligned with the surge axis of the device were considered.

STAR-CCM+'s unsteady Reynolds-averaged Navier–Stokes (URANS) model was used with a $k-\omega$ turbulence closure on a finite-volume mesh. A second-order unsteady solver was employed. A VOF model was used to accommodate the multiphase flow and track the free surface.

Further details on this model are presented in the subsequent subsections. The definition of the computational domain and its boundaries is described in Sect. 2.3.1. Discussion on the selected timestep and meshing, based on the flow properties of each simulation case, are provided in Sect. 2.3.2. Additionally, wave damping near the outlet boundary (Sect. 2.3.3), motion capturing (Sect. 2.3.4), and dynamics modeling (Sects. 2.3.5, 2.3.6) are discussed.

2.3.1 Computational domain

A layout diagram of the computational domain for simulations of the Triton device is shown in Fig. 6. Velocity

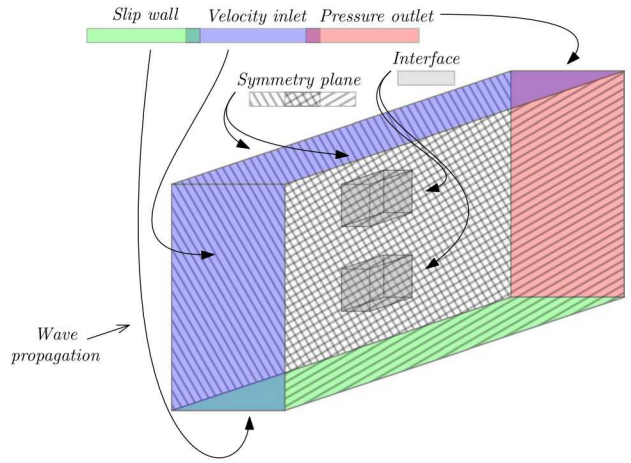

Fig. 6 Dimensions of computational domain for CFD simulation of Triton WEC

inlets, in which the fluid velocity and volume fraction are controlled, are shown in blue and were utilized on front and top boundaries. Symmetry planes, shown with hash patterns, were utilized on the side boundaries. A pressure outlet, where the hydrostatic pressure of a still water condition is specified to promote wave damping, is shown in red and located at the rear of the domain. A slip wall was utilized on the bottom of the domain, which was always located sufficiently far from the free surface to minimize flow in its vicinity (see Table 2 in Sect. 2.3.2 for further information on domain sizing). The interface boundaries for two separate inner overset domains, one for the float and one for the reaction ring, are shown in gray (see Sect. 2.3.4 for more on overset domains).

2.3.2 Spatial and temporal discretization

An unstructured tetrahedral mesh was utilized for the CFD simulations. Figure 7 shows a parametric definition of the computational domain and the various mesh refinement regions within. In addition to a mesh refinement region to capture the free-surface interface, an overlapping wave zone region was defined to capture wave fluid motion. Two additional refinement regions were defined around the expected travel of the float and reaction ring bodies to resolve more complex flows and support overset mesh interpolation.

Within the free-surface refinement zone, mesh sizing was based on wave length, λ, and wave height, H. As per guidance from STAR-CCM+, the cell length, Δx, was generally set such that $n = \lambda/\Delta x > 100$. Similarly, cell height, Δz, for the free-surface zone was set for $m = H/\Delta z > 40$. The wave zone mesh refinement spacings were generally set at two times that of the free-surface zone. The float and reaction ring refinement zones were roughly equivalent to those in the free-surface zone.[2] The exact dimensional and nondimensional mesh spacings for each simulation are reported in Table 2.

In addition to having sufficient resolution to resolve flow features, the spatial and temporal resolution must also respect the Courant–Friedrichs–Lewy (CFL) number (Courant et al. 1928):

$$\mathrm{CFL} = \frac{u\Delta t}{\Delta x}. \tag{1}$$

This nondimensional number defines the number of cells through which fluid particle will move within a single time step. This is often used to enforce a condition based on fluid velocity. However, we can also consider the transport of additional quantities in terms of CFL. For a free-surface flow, we must, for example, consider the volume fraction or free-surface interface.

For a free-surface wave, the spatial (Δx) and temporal (Δt) discretization must be such as to capture the phase velocity of the wave ($v_\mathrm{p} = \lambda/T$). Setting the velocity in (1) to the wave phase velocity ($u = v_\mathrm{p}$) and recalling that we have defined the horizontal mesh spacing as $n = \lambda/\Delta x$, we can write

$$\mathrm{CFL}_{v_\mathrm{p}} = \frac{v_\mathrm{p}\Delta t}{\Delta x}, \tag{2a}$$

$$= \frac{\lambda\Delta t}{T\Delta x}, \tag{2b}$$

$$\rightarrow \Delta t = \frac{\mathrm{CFL}_{v_\mathrm{p}} \cdot T}{n}. \tag{2c}$$

It is suggested by Star-CCM+ to maintain $\mathrm{CFL}_{v_\mathrm{p}} < 0.5$ for free-surface flows; the time steps summarized in Table 2 are based on this condition. In addition to phase velocity, we also consider the vertical velocity of the free surface, as given by $\dot{\eta} = 2H/T$. Thus, we can also maintain $\mathrm{CFL}_{\dot{\eta}} = \dot{\eta}\Delta t/\Delta z < 0.5$. Note that, for the meshes used here, it was generally true that $\mathrm{CFL}_{\dot{\eta}} < \mathrm{CFL}_{v_\mathrm{p}}$.

Adjacent to the hulls of the Triton's float and reaction ring, body-fitted prism layer meshes (e.g., Vinokur 1983) were utilized to capture the boundary layer. Instead of resolving the viscous sublayer, an "all-y^+" wall treatment, in which wall functions are used to obtain the boundary conditions for the continuum equations, was applied. For both

[2] Since the flow within most of the domain is primarily planar, the desired mesh spacings generally result in cells with somewhat large aspect ratios within the background domain. In contrast, the flow around the float and reaction ring is more three-dimensional, as such, the mesh configuration was adjusted in these zones to achieve lower aspect ratio cells.

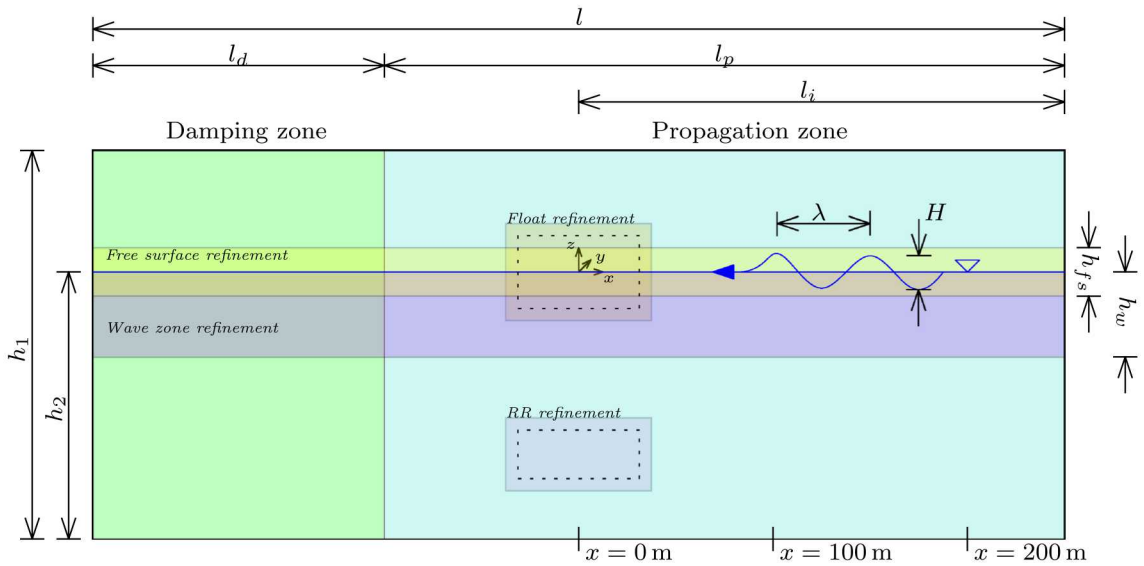

Fig. 7 Domain setup for Triton CFD simulation. Mesh refinement regions (free surface, float, and reaction ring "RR") are shown along with damping and wave propagation zones

the float and reaction ring, prism layer cells were sized to achieve a $y^+ \approx 150$ at the first cell centroid based on flat-plate boundary layer theory (e.g., Schetz 1993). Figure 8 shows a cross-sectional plane of the boundary layer cells around the reaction ring.

2.3.3 Wave damping

One issue with free-surface-resolving CFD simulations is the handling of wave reflections at boundaries. Since wave flow is oscillatory (in the first-order approximation, the particle paths are perfectly orbital), it cannot easily be handled by a simple pressure outlet boundary condition. This issue is especially challenging for a simulation with no forward speed component, such as those of WECs and offshore platforms. Here, we have employed a damping zone on the pressure outlet boundary to alleviate this problem. Figure 7 shows the wave propagation and damping zones in the domain; the lengths of these zones are given in Table 2. Within the damping zone, vertical velocity is subject to an artificial resistance term, which increases quadratically in space as one moves toward the pressure outlet boundary (Choi and Yoon 2009).

Thus, the waves within the propagation zone shown in Fig. 7, including the diffracted and radiated waves, will be damped as they move into the damping zone. The waves should ideally reach zero amplitude before reaching the pressure outlet boundary. The damping zone should have a similar effect as a physical beach in a wave tank.

2.3.4 Motion capturing

The motion of the Triton's float and reaction ring were enabled via the use of overset meshes. STAR-CCM+ uses an unstructured overset mesh formulation (Hadzic 2006). For this, three mesh regions were defined: a background mesh that includes external boundaries and represents the "virtual wave tank"; an overset domain that tracks the float; and an overset domain that tracks the reaction ring. Figure 9 shows a rendering of the computational mesh at the symmetry plane. Here, the two overset regions' meshes (float and reaction ring) are shown in red while the background domain mesh is shown in blue.

The overset approach allows the background mesh to remain fixed in space. This is beneficial since the detailed free-surface meshing discussed in Sect. 2.3.2 remains aligned with the free surface regardless of the device motion. A linear interpolation scheme was used to pass the solution between the background domain and the two overset domains. As shown in Fig. 7, refinement zones were used to maintain similar mesh sizes at the interpolation interface (i.e., in both the overset and background domain meshes).

2.3.5 PTO/tendons

The reaction forces on the float and reaction ring bodies due to the three PTO tendons were calculated based on a simple vector analysis. Assuming that a tendon between the bodies remains taut and directly connects the PTO on the float to the mounting point on the reaction ring, we can write

Table 2 Summary of CFD model domain, mesh, and timestep settings

		SS01-R	SS01-F	SS02-R	SS02-F
Wave parameters					
Wave period	T (s)	9.2		16.2	
Wave frequency	f (Hz)	0.11		0.06	
Wave height	H (m)	9.0	7.5	9.9	7.5
Wave length	λ (m)	132		410	
Wave number	k (rad/m)	0.048		0.015	
Phase velocity	c_p (m/s)	14		25	
Group velocity	c_g (m/s)	7		13	
Domain geometry					
Domain height	h_1 (m)	190	475	475	475
Water depth	h_2 (m)	150	400	400	400
	h_2/λ	1.1	3.0	1.0	1.0
Domain length	l (m)	550	660	2500	2500
	l/λ	4.2	5.0	6.1	6.1
Damping zone length	l_d (m)	150	0	810	0
	l_d/λ	1.1	0.0	2.0	0.0
Prop. zone length	l_p (m)	400	660	1690	2500
	l_p/λ	3.0	5.0	4.1	6.1
Init. zone length	l_i (m)	275.0	330.0	1250.0	1250.0
	l_i/λ	2.1	2.5	3.1	3.1
Free-surface zone height	h_{fs} (m)	10	12	12	12
	h_{fs}/H	1.11	1.60	1.21	1.60
Wave zone height	h_w (m)	50	100	100	100
	h_w/H	5.56	13.33	10.10	13.33
	h_w/λ	0.38	0.76	0.24	0.24
Mesh, time step, solver					
Free surf. zone cell length	Δx_{fs} (m)	1.00	1.00	4.00	4.00
	$\lambda/\Delta x_{fs}$	132	132	102	102
	CFL_{v_p}	0.18	0.07	0.1	0.1
Free surf. zone cell height	Δz_{fs} (m)	0.10	0.25	0.25	0.25
	$H/\Delta z_{fs}$	90	30	40	30
	$\mathrm{CFL}_{\dot{\eta}}$	0.12	0.02	0.03	0.02
Time step	Δt (s)	0.0125	0.0050	0.0125	0.0125
	$T/\Delta t$	736	1840	1296	1296
Cell count					
Total	–	3.6E+07	1.4E+07	5.6E+06	5.6E+06
Overset, float	–	1.9E+06	1.2E+05	3.6E+04	3.6E+04
Overset, reaction ring	–	8.5E+04	6.6E+05	6.6E+05	6.6E+05
Background	–	4.3E+07	1.1E+07	2.1E+06	2.1E+06

$$\mathbf{r} = \mathbf{p}_f - \mathbf{p}_{rr} \tag{3}$$

for the vector along which reaction forces will occur. Here, as shown in Fig. 5, $\mathbf{p}_f$ and $\mathbf{p}_{rr}$ are the tendon attachment points on the float and reaction ring, respectively.

Two reaction components must be modeled for each PTO/tendon: damping and spring stiffness. Since the stiffness of the tendons themselves is so high, the overall tendon stiffness effect is dominated by that applied by the PTO. The spring component of the PTO is determined for a positive stiffness constant of k_{PTO} and acts along the tendon:

$$\mathbf{F}_{\mathrm{spring}} = -k_{\mathrm{PTO}}\left(|\mathbf{r}| - l_0\right)\hat{\mathbf{r}}, \tag{4}$$

where $\hat{\mathbf{r}}$ represents the unit vector of $\mathbf{r}$. The nominal length of the tendon, at which the spring force would be zero, is represented by l_0. Note that no consideration is given for slack conditions and snap loading.

Similarly, the damping component from the PTO can be expressed in terms of a PTO damping constant b_{pto}.
The rate change in the vector between the PTO on the float to the mounting point on the reaction ring is

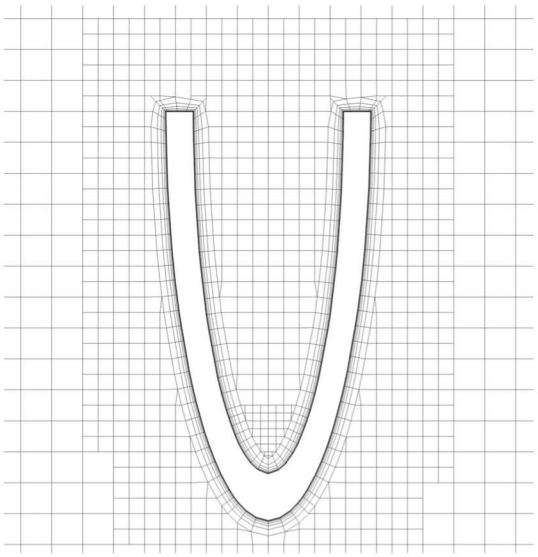

Fig. 8 Cross section showing body-fitted boundary layer cells around the Triton reaction ring

$$\mathbf{v} = \mathbf{v}_f - \mathbf{v}_{rr}. \tag{5}$$

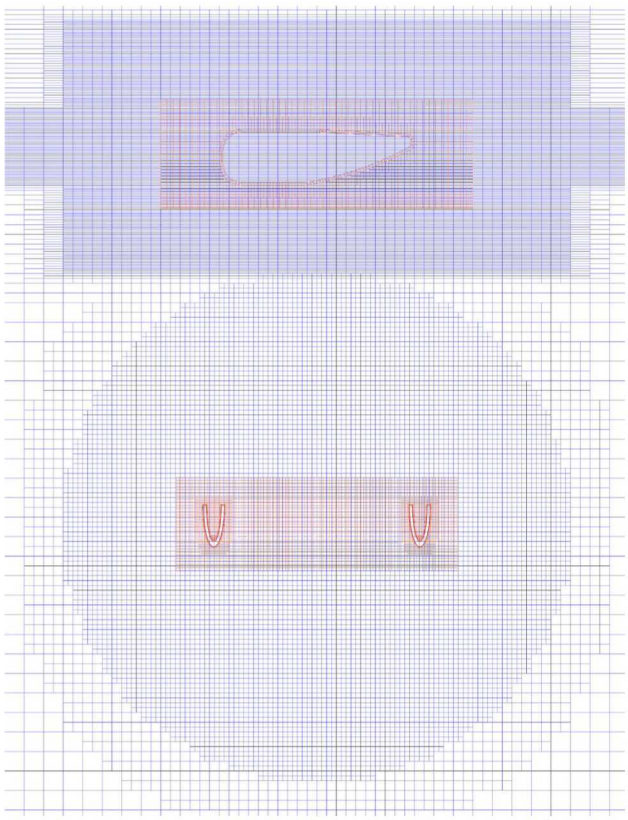

Fig. 9 Rendering of computational mesh at symmetry plane. Overset domain meshes (float and reaction ring) are shown in red. Background domain mesh is shown in blue (color figure online)

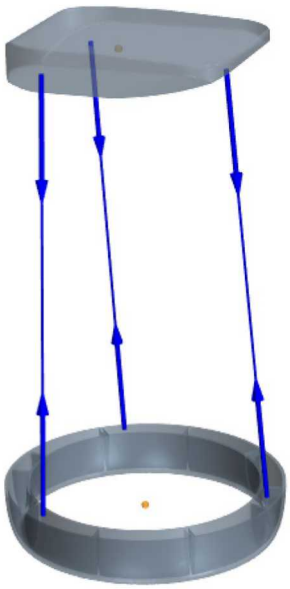

Fig. 10 Visualization of tendon lines and forces of Oscilla Triton float and reaction ring

To find the magnitude of the PTO damping, we use the scalar projection of the velocity onto the tendon vector:

$$q = \mathbf{v} \cdot \hat{\mathbf{r}}. \tag{6}$$

Similarly, the vector projection is defined as

$$\mathbf{q} = q\hat{\mathbf{r}}. \tag{7}$$

From these, the magnitude of the PTO damping force can be found:

$$F_{\text{damp}} = -b_{\text{pto}}\max(q, 0). \tag{8}$$

Note that the max expression prevents a damping force from being applied as the tendon shortens. The PTO damping force vector is thus given by

$$\mathbf{F}_{\text{damp}} = F_{\text{damp}}\hat{\mathbf{r}}. \tag{9}$$

PTO/tendon reactions between the two bodies were implemented via a series of field functions within STAR-CCM+. Field functions were defined for finding the time-dependent tension in the Triton's port and forward tendons. Since symmetry was utilized, the starboard tendon was not modeled and the forward tendon is bisected by the symmetry plane and thus, only half of the tension in that tendon was applied in the model. Using opposite signs, the force vector of each tendon tension was applied at the PTO connection points. A visualization of the tendon lines and the forces imparted by their tensions at the PTO connection points is shown in Fig. 10.

2.3.6 Mooring lines

Mooring lines were assumed to act as linear springs in the horizontal frame. Since a symmetry plane was applied, only

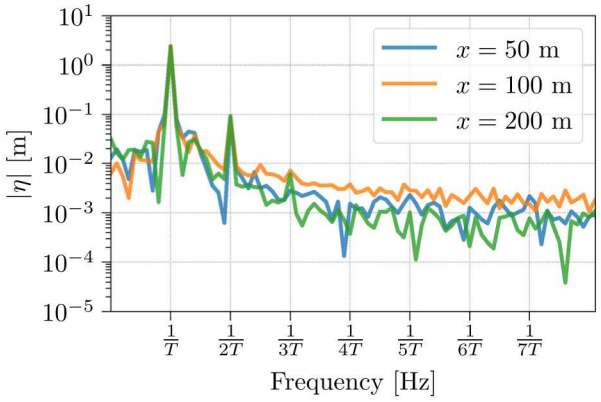

Fig. 11 Free surface wave gauges from quasi-2D SS02-R simulation taken at $x = 50,\ 100,\ 200$ m (see locations in Fig. 7)

a single spring (in the x-axis) was required. Based on the full mooring system design, this was modeled as a 26 kN/m stiffness spring with 79 kN of pretension (shown in Fig. 5 as k_m). The spring was modeled to be acting at the float center of gravity and, therefore, does not restrict pitch rotation of the float.

3 Results

3.1 Using regular design waves

3.1.1 Benchmarking

To test the performance of the mesh and solver settings utilized, a series of benchmarking simulations were run. First, using a quasi-2D domain, a series of simulations were run to refine the mesh to better capture the surface waves. These quasi-2D domains have the same dimensions as that shown in Table 2, but are only one cell thick along the y-axis (transverse to wave propagation).

Here we consider results for the SS02-R case. Utilizing this quasi-2D approach, the domain for this simulation has only 8.4×10^4 cells (roughly 1% that of the full SS02-R mesh). To assess the suitability of the mesh, solver settings and, boundary conditions, the simulated wave profile was tracked as a function of both time and space. Figure 11 shows the discrete Fourier transform of the wave time history for $x = 50,\ 100,\ 200$ m (see locations in Fig. 7). We can see that the wave contains some nonlinear content at the second harmonic, as would be expected for a wave of this steepness, but this harmonic's amplitude is less than 10% that of the first harmonic.

Figure 12 shows an alternative means of analyzing the accuracy of this same simulated wave. Here, the wave-free surface is shown at a longitudinal transects at different instances throughout the solution (0 s, 16.2 s, and 162 s). A

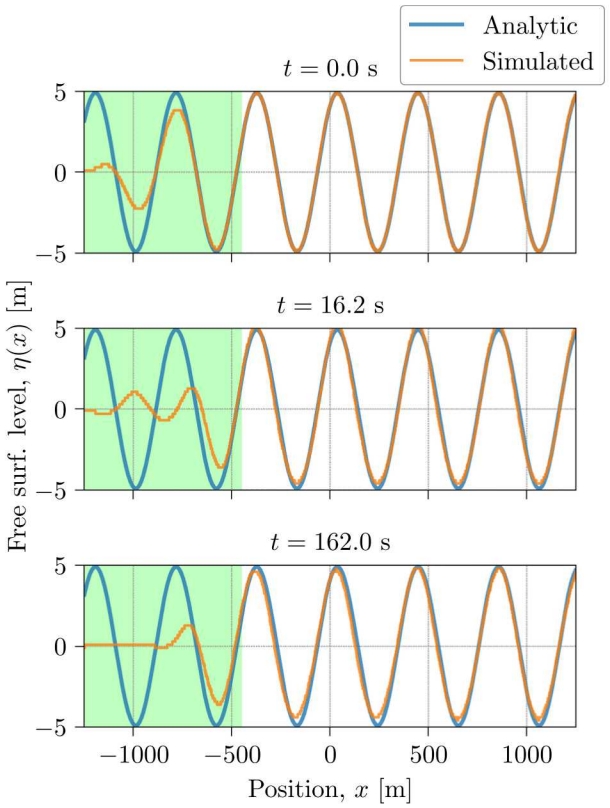

Fig. 12 Free surface of simulated SS02-R wave taken at $t = 0,\ 16.2,\ 162$ s ($t = [0,\ 1,\ 10] \cdot T$) during solution shown with analytic wave solution. Damping zone marked with green

Stokes first-order wave is shown in Fig. 12 for comparison, as this order wave is used in the OrcaFlex model. Note that the damping zone, as discussed in Sect. 2.3.1, is shaded in green in Fig. 12. From Fig. 12, we can see good agreement between the simulation and first-order wave. We can see that at $t = 162$ s (after 10 periods of waves), the simulated wave has the rounder trough and sharper crest that we recognize from higher order waves.

We can further quantify the degree to which the simulated wave matches the target wave by the normalized root-mean square error:

$$\text{FIT} = \left(1 - \frac{\|s_e - s_v\|_2}{\|s_e - \bar{s}_e\|_2}\right) \cdot 100. \tag{10}$$

Considering the free surface time series at $x = 50$ m using (10), we find FIT = 88.0%.

3.1.2 SS01-R

Figure 13a shows the position, orientation, and tendon tension responses for SS01-R. A rendering from the simulation

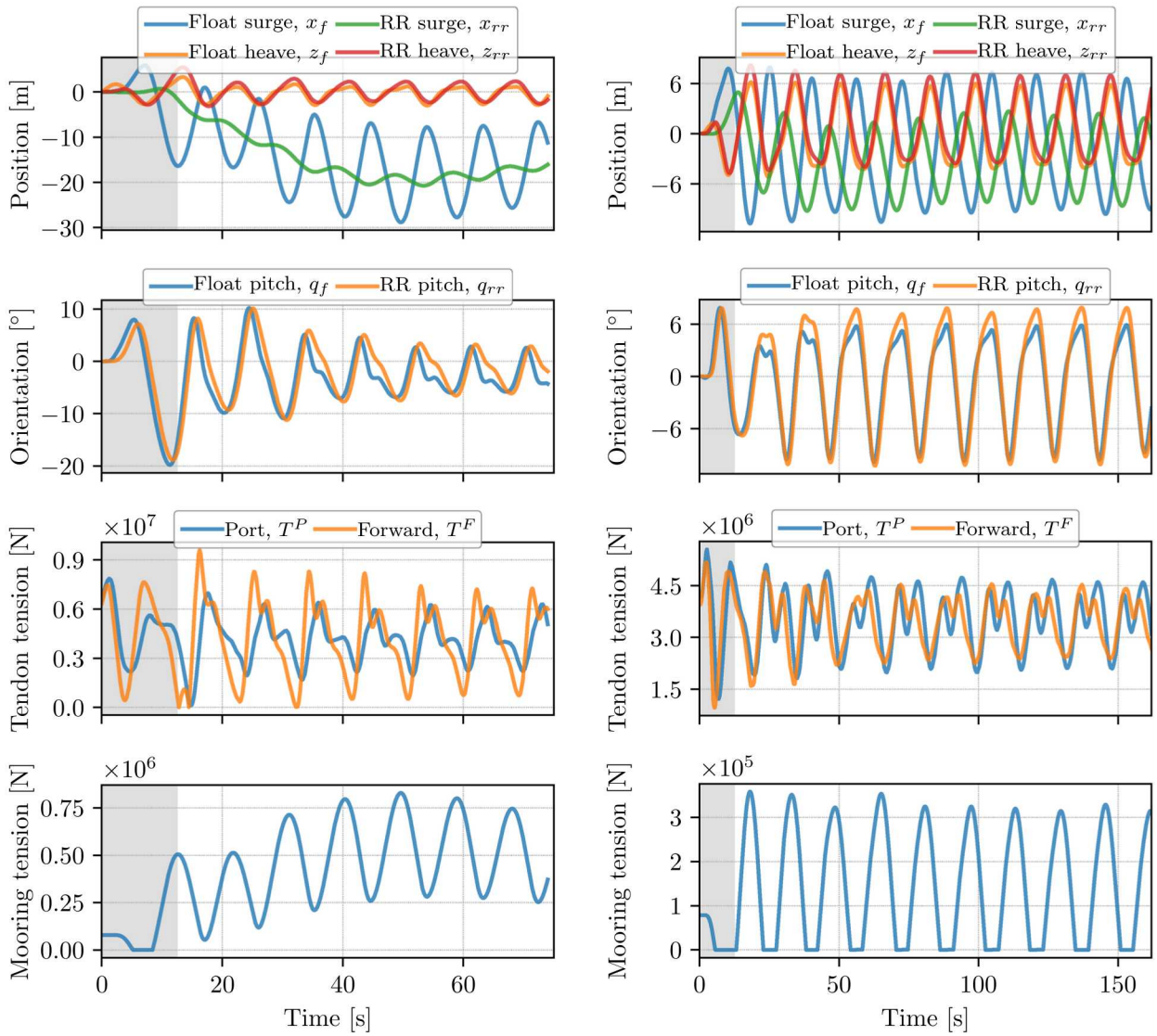

Fig. 13 Regular-wave case responses. Note that gray region ($0 \le t \le 10$ s) indicates dynamics ramping. All plots use the same time axis

at $t = 60$ s is shown in Fig. 14. Note that to ensure stability, a ramping under-relaxation of the motion of the WEC was enforced at the beginning of the simulation. In Fig. 13a, the period of dynamic ramping ($0 \le t \le 10$ s) is shown in gray. In this simulation, the maximum tension in the port and forward tendons were 6.4 MN and 8.3 MN, respectively. Referring back to Table 1, we can see that a maximum tendon load of 8.8 MN was predicted in the OrcaFlex model. Note that these maximum values for the CFD simulation are taken after the motion becomes periodic (for $t > 18$ s in SS01-R). The mooring tension looks to top out at 0.8 MN when we account for some low-frequency dynamics excited by the initialization procedure (see Fig. 13a). This also agrees fairly well with the OrcaFlex model prediction of 0.7 MN.

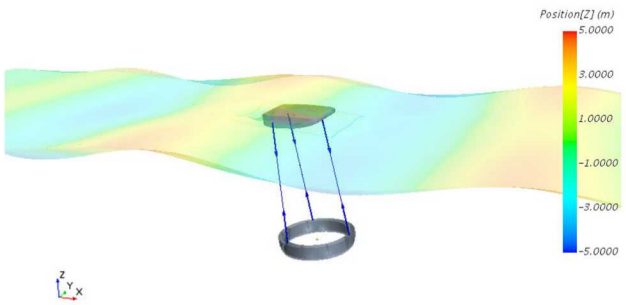

Fig. 14 Rendering from SS01-R regular-wave case ($H = 9.0$ m and $T = 9.2$ s) at $t = 60$ s

Note that at $t \approx 14$ s a slack event in the forward tendon occurs. This is visible in the behavior of the tendon tension plot shown in Fig. 13a, where the curve appears to follow something like an absolute value function upon approaching

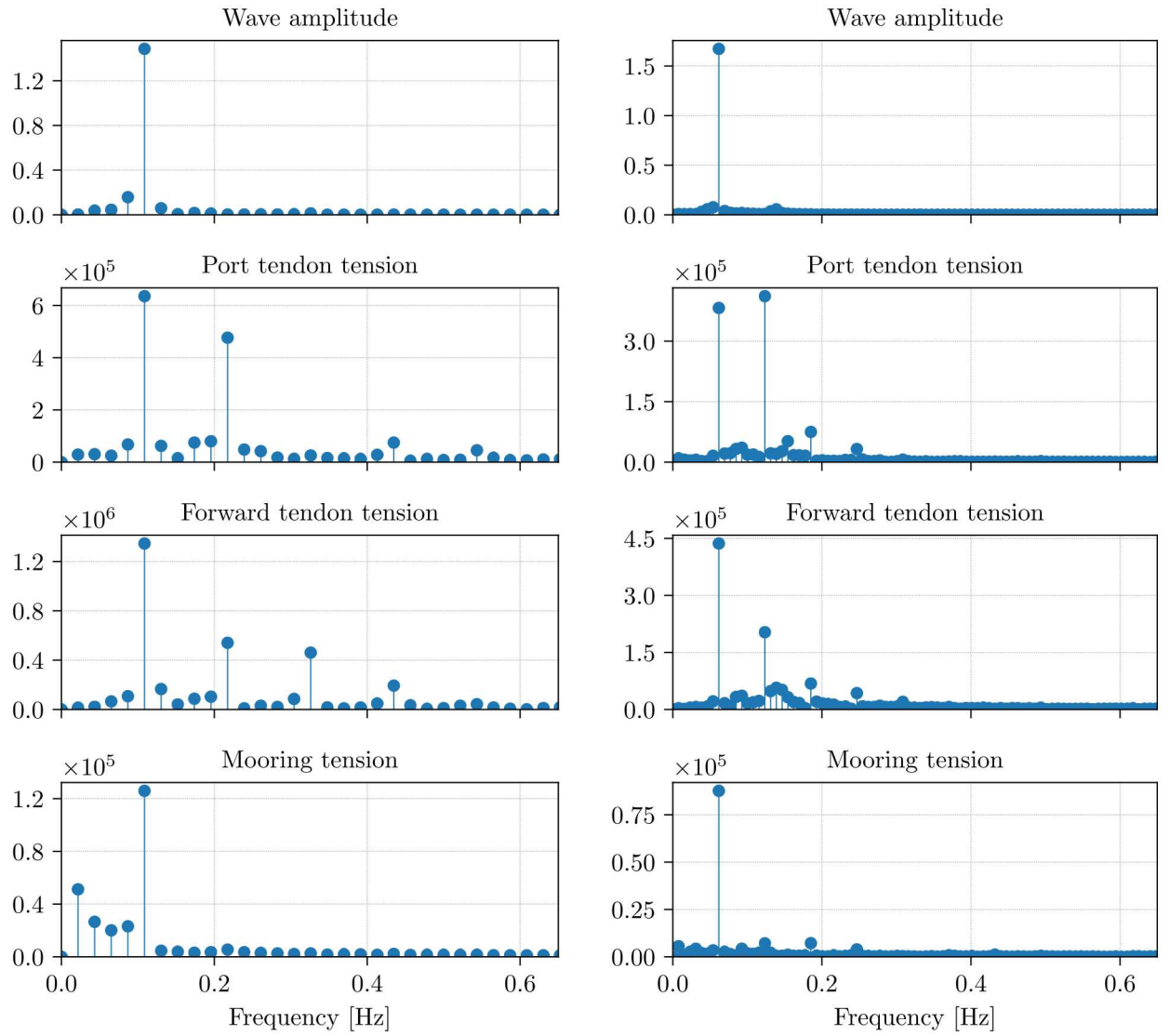

(a) SS01-R **(b)** SS02-R

Fig. 15 Regular-wave case Fourier analyses

zero. As discussed in Sect. 2.3.5, the formulation applied here does not account for slack and snap loading, so the dynamics of this event are not well captured. Regardless, this event occurs just after the dynamics ramping period, but does not reoccur after that. Thus, it is believed that this slack line event is mostly an artifact of the initialization and ramping procedure and not of particular importance for this simulation. We also observe a slack event in the mooring tension during the initialization period.

Figure 15a shows the discrete Fourier transform of the tendon and mooring responses taken from five periods starting a $t = 18$ s. It is clear from both Figs. 13a and 15a that the tendon tension response is highly nonlinear in this regime. Total harmonic distortion (THD) is one measure of nonlinearity and can be defined as

$$\mathrm{THD} = \frac{\sqrt{R_2^2 + R_3^2 + R_4^2 + \cdots}}{R_1}, \tag{11}$$

where R_n is the RMS amplitude of nth harmonic. With the fundamental frequency $n = 1$, each subsequent harmonic's frequency being $f_n = nf_1$. For this case, the fundamental frequency is $f_1 = T^{-1} = 0.109$ Hz. The input signal, in this case the wave, has THD = 4%. The forward and port tendons have THDs of 54% and 74%, respectively (i.e., more than half of the energy content occurs at superharmonics of

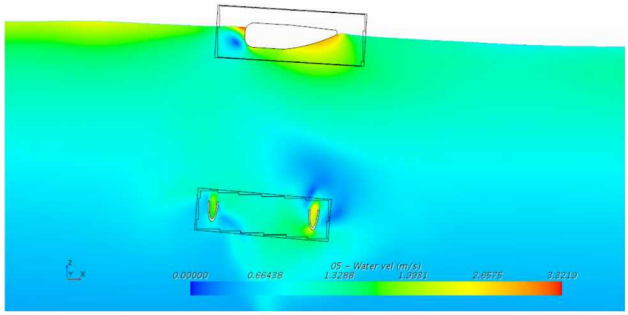

Fig. 16 Water velocity magnitude for SS02-R regular-wave case at $t = 161.7$ s. Rendering also shows interfaces for overset regions around the float and reaction ring

the input). The mooring tension response in this case has THD = 5%. Note that THD is not a complete measure of nonlinearity in a response. For example, Fig. 15a shows a large amount of low-frequency content in the mooring tensions response, which is not accounted for in the THD calculation.

3.1.3 SS02-R

Figure 13b shows the response from the SS02-R regular-wave case. Figure 16 shows a rendering of the water velocity magnitude from SS02-R at $t = 161.7$ s (at the end of the simulation). After initialization, the tendons remain consistently in tension with a maximum tension force of roughly 5 MN. The maximum mooring tension (after the initialization artifacts have passed) is roughly 0.3 MN. From Table 1, the OrcaFlex model predicted a much larger mooring tension of roughly 0.9 MN in this irregular sea state. This disagreement is perhaps not too surprising, as discussed in Sect. 2.3.6, as the mooring model implemented in these CFD simulations is not as complex as that used in OrcaFlex. We also notice that the mooring line is going slack with every period. The maximum tendon tension from the CFD simulation was roughly 4.7 MN; OrcaFlex predicted a maximum tendon tension of 7.2 MN. This is a relatively large difference as well, which, as will be discussed in Sect. 5, may demonstrate a shortcoming of the equivalent regular design wave.

As with SS01-R, a spectral analysis was performed on the responses of interest for SS02-R. The results of this analysis are shown in Fig. 15b. For this spectral analysis, the response signals for $30 \leq t \leq 159.6$ s (exactly eight wave periods) were used. The wave amplitude had THD = 1%, which is lower than SS01-R (which is a steeper wave, and thus expected to be more nonlinear). The forward and port tendons have THDs of 110% and 50%, respectively. As can be seen in Fig. 15b, the port tendon tension response has a very strong 2nd harmonic excited in this wave. The mooring tension response in SS02-R had THD = 12%; this is slightly larger than in SS01-R.

3.2 Using focused design waves

Figure 17a, b shows the time realizations of the SS01-F and SS02-F focused waves, respectively. Both the target wave (that was calculated using linear wave theory) and the simulated wave from a quasi-2D simulation (no device) are shown. The simulated waves match the target wave quite closely, particularly in the case of SS02-F (shown in Fig. 17b). The agreement for SS01-F (shown in Fig. 17a) is less close. Applying (10), the simulated waves in SS01-F and SS02-F match their target waves with FIT = 65% and FIT = 93% at $x = 0$ m, respectively.

This larger error in SS01-F is likely because SS01-F is steeper than SS02-F, which has two major repercussions in terms of this simulation: (1) nonlinear wave dynamics will play a larger role in the steeper wave (note that the MLER formulation uses linear wave theory) and (2) breaking and spilling will occur due to properly simulated physics but also due to spatial discretization at the instantaneous free surface.

The device responses from SS01-F are shown in Fig. 18a. Similarly, the device responses from SS02-F are shown in Fig. 18b. We can see a similar pattern in the translation and orientation responses of the float and reaction ring for both SS01-F and SS02-F. In SS01-F, the heave position of the float and reaction ring show a similar ringing response. The surge position of the reaction ring in SS01-F shows a mostly low-frequency response, while some ringing is excited in SS02-F. In both cases, the float and reaction ring experience large negative pitch (bow up) responses at the focus time, which slowly decay.

The tendon tensions show somewhat different behaviors in SS01-F and SS02-F, with a large positive spike in SS01-F and a large negative spike (from the mean) in SS02-F. This is likely due to the phasing of the float surge response, which has a large negative spike at the focus time in SS02-F. The mooring tensions in these simulations are fairly different. As with SS02-R, we see slack mooring events in SS02-F.

Note that in addition to the responses predicted by the CFD simulations, the MLER predicted response based on linear theory (originally shown in Fig. 4) are shown in Fig. 18 by dashed curves. The magnitude of the tendon tension response maximum predicted by the MLER method was closely reproduced in the CFD simulation. However, the CFD and MLER response time histories are slightly out of phase. The maximum tendon tension occurs slightly before the targeted time. Looking back at Fig. 17a, we can recall that the simulated SS01-F wave did not perfectly track the target wave, likely leading to this discrepancy. The CFD and

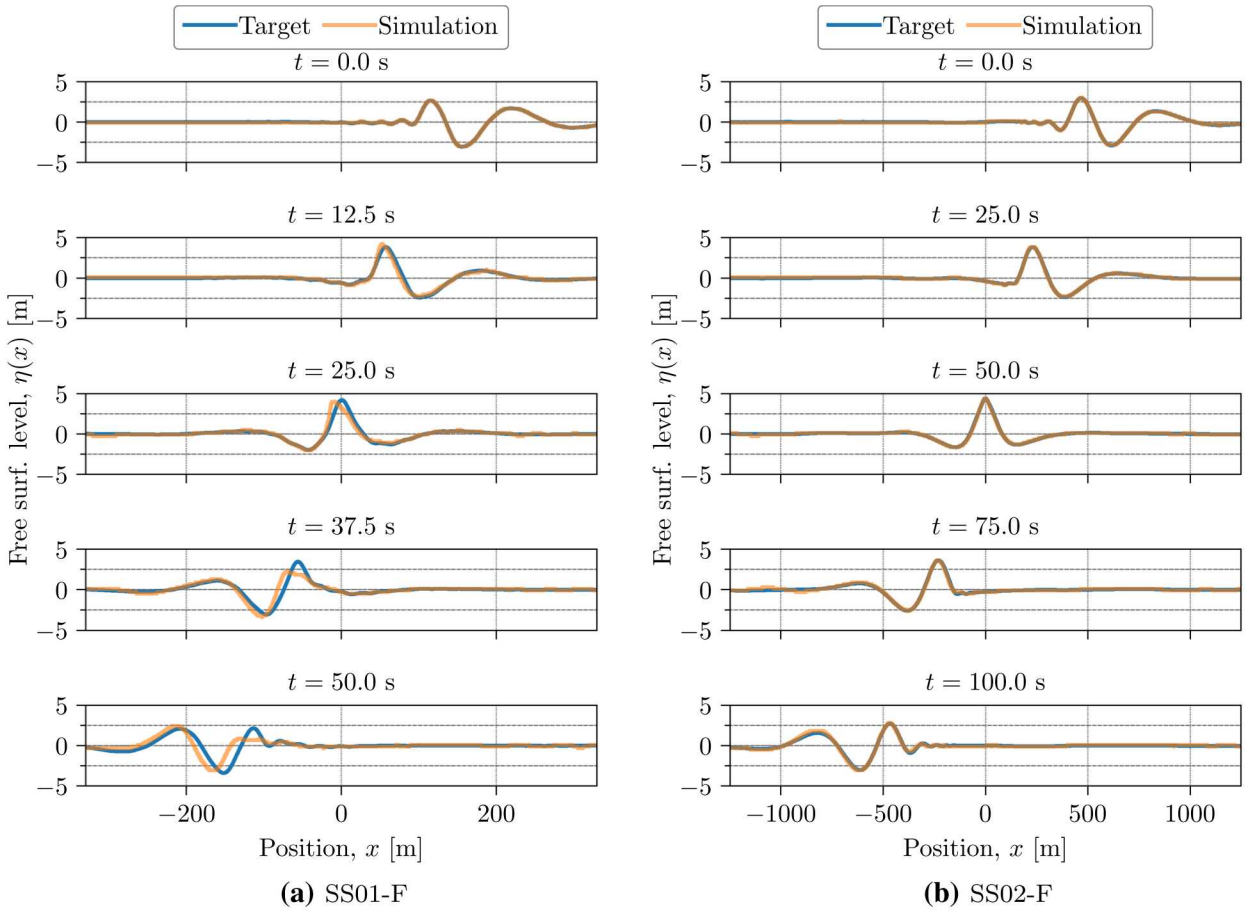

Fig. 17 Focused-wave target and simulated waves

MLER responses in SS02-F are more aligned in phase, but the magnitudes are off, particularly in the oscillations after the focus point. In both wave cases, we see that the CFD response is more complex than those predicted by the linear MLER method.

4 Discussion

Table 3 shows a summary of the responses of interest from the equivalent regular and focused-wave CFD simulations. Additionally, results from the OrcaFlex model are shown. The percentile for predictions from the regular and focused-wave CFD simulations in comparison to the irregular Orcaflex simulation are shown in parentheses. For example, in the case of SS02, the equivalent regular and focused design wave CFD simulations gave maximum tendon tensions of 4.73 MN and 5.81 MN, respectively. Comparing these values set of relevant to the entire 3-h Orcaflex simulations, the CFD predictions rank at 77.55% and 97.60%, respectively. Thus, we can see that although the maximum value from the Orcaflex simulation (7.16 MN) is much greater than those from the shorter CFD simulations, this a long tail behavior (since 97.60% of the values are actually lower than 5.81 MN).

In addition, the complementary cumulative distribution functions (CCDFs), which are sometimes reference to survival functions, are shown in Fig. 19:

$$\mathrm{CCDF}_X(x) = P(X > x) = 1 - F_X(x), \tag{12}$$

where $P(X > x)$ is the probability that the response, X, will take a value greater than x. The cumulative distribution function is $F_X(x)$. To better investigate behavior in the tail region, we thus consider the CCDF. The tendon tension responses are shown in Fig. 19a and the mooring tension responses are shown in Fig. 19b. The curves are shown for the CCDFs from the Orcaflex results for both the SS01 and SS02 cases. Additionally, vertical lines are shown for the results of the CFD simulations, with the regular-wave results shown by dashed lines and the focused-wave results shown by dash-dot lines.

It is important to note that the approaches compared in Table 3 and Fig. 19 have a number of differences. Each case uses a different approach to represent the sea state of

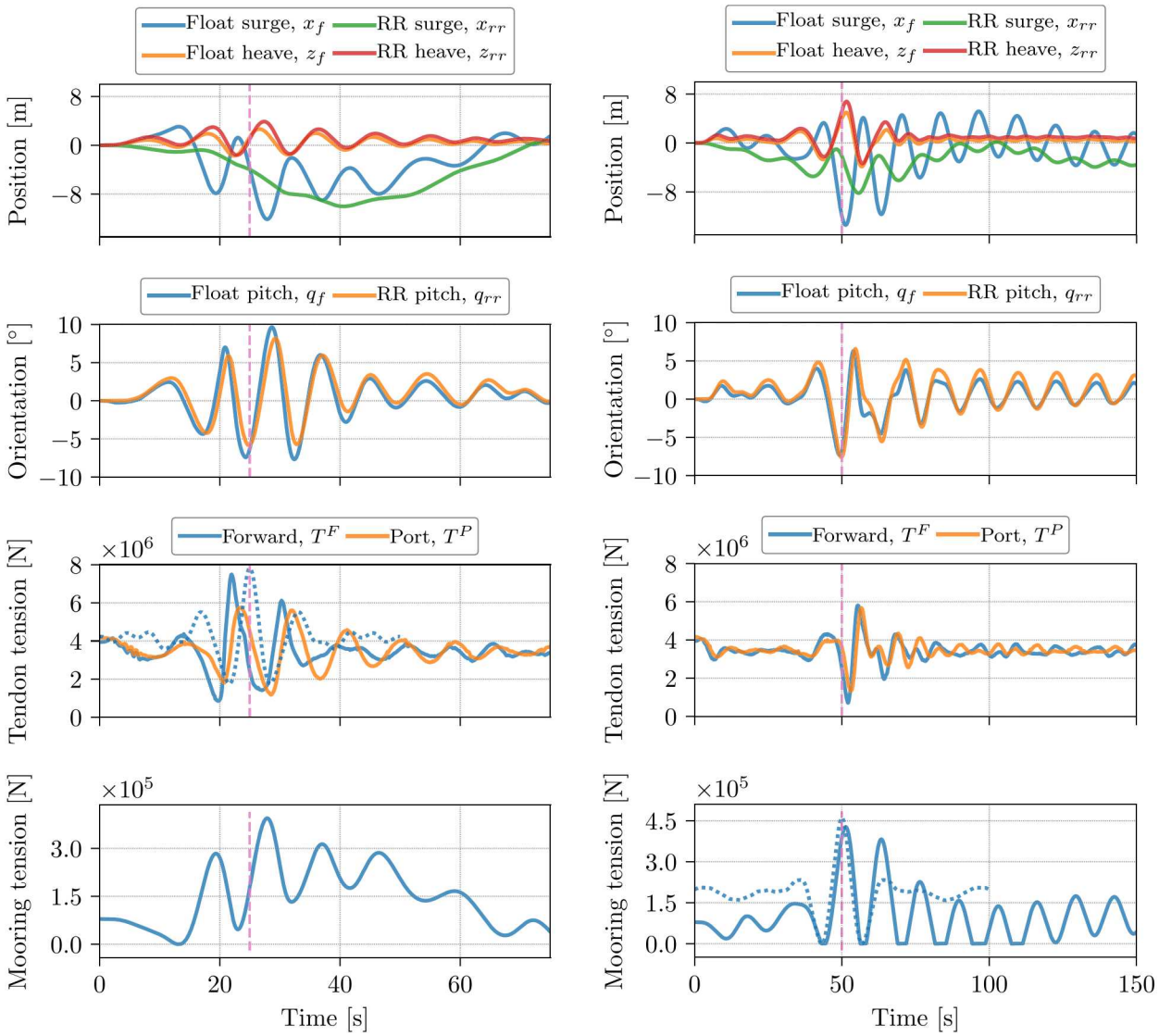

(a) SS01-F **(b)** SS02-F

Fig. 18 Focused-wave device responses. Vertical pink dashed lines indicate the focused-wave peaks. Dotted curves show MLER predicted responses (color figure online)

Table 3 Tendon and mooring tension results with percentile from irregular OrcaFlex prediction in parentheses

Sea state	Tendon tension (MN)			Mooring tension [MN]		
	CFD-equiv. reg.	CFD-focused	OrcaFlex	CFD-equiv. reg.	CFD-focused	OrcaFlex
SS01	8.27 (99.99%)	7.49 (99.68%)	8.76	0.819 (100.0%)	0.394 (91.38%)*	0.699
SS02	4.73 (77.55%)	5.81 (97.60%)*	7.16	0.320 (69.56%)	0.428 (88.50%)	0.857

Results for which focused MLER waves are *not* designed for are marked with *

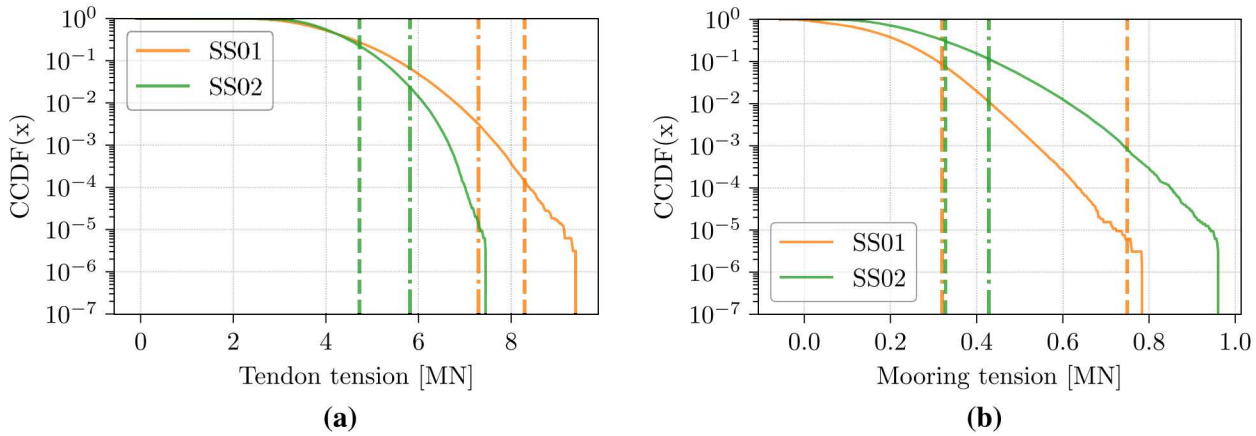

Fig. 19 Complementary cumulative distribution functions (CCDFs) along with the results from CFD simulations shown by vertical lines. Regular-wave results are shown by dashed lines (- - -); focused-wave results are shown by dash-dot lines (- · -)

interest. In the CFD simulations, the sea state is reduced, either to a single regular wave or to a focused wave. Conversely, in the OrcaFlex simulation, the sea state is simulated as an irregular time series with random phasing to realize 3 h of non-repeating waves. Additionally, it is important to recall that the focused MLER waves are designed to target a specific response (SS01-F is designed to target tendon tension and SS02-F is designed to target mooring tension). The results for the responses which these focused waves are *not* designed for are marked with * in Table 3.

As previously mentioned, the agreement between the maxima predicted by the various modeling approaches is mixed. The predictions from the CFD simulations generally under-predict the maxima from OrcaFlex simulations. However, looking more closely at the CFD predictions percentiles with respect to the irregular responses predicted in OrcaFlex, we can see a more encouraging trend. For all of the SS01 cases, the CFD predictions have a percentile greater than 90%. The percentiles for the longer period SS02 are lower. In general, the predictions of tendon tension are better (higher than 97% in all but one case). The mooring tension is much more widely spread, ranging from 70 to 100%. This may be due to the overly simplified mooring system modeling approach. It could also be a result of the lower frequency nature of the mooring response, which may not have had adequate time to develop in the CFD simulations.

5 Conclusion

In this study, the response of the Triton wave energy device was assessed in a set of key operational sea states where extreme loading is expected. These sea states were selected based on a large set of mid-fidelity model simulations and were then evaluated at high fidelity with a model that utilizes CFD. This CFD model incorporates a representation for the tendon and PTO dynamics connecting the two bodies of the Triton and a simplified model for the mooring system. To enable the irregular sea states of interest to be evaluated in the CFD model in a timely manner, equivalent regular-wave and focused-wave representations were represented and evaluated.

Referring back to Table 3, the focused-wave representation predicted larger loads than the equivalent regular wave for SS02 but not as strongly for SS01, suggesting that the focused-wave methodology could be further refined. However, the focused waves gave predictions that were more consistently at a higher percentile with respect to the irregular OrcaFlex predictions than the regular-wave predictions. The equivalent regular wave struggled most for the longer wave period case (SS02-R), which may indicate that these larger loads were tied to higher frequency energy in the irregular-wave spectrum (which is not included in the equivalent regular design wave). Conversely, the focused waves contain a broader range of energy content, and in some respects resemble an impulse, in theory allowing for broader band responses.

Future work on the CFD model should consider more complex system dynamics, such as that of the mooring system. This will likely require coupling with external models, such as OrcaFlex. However, this is a necessary step to bring the rest of the WEC system dynamics modeling up to par with the fidelity of the CFD model. Additionally, while only a simple PTO control was considered in this study, it may be necessary in future studies to include a more complete, complex control implementation for such CFD models. This can be accomplished via function calls to custom libraries,

but coupling with a tool such as MATLAB Simulink would be more flexible and functional.

Finally, it is expected that physical model tests will give a useful indication of system design loads for the full-scale device. Tank tests have recently been conducted for the Triton device and, in a future study, these results will be compared to the mid- and high-fidelity model results that were presented in this article.

Acknowledgements This material is based upon work supported by the U.S. Department of Energy under Award Number DE-EE0007346. Sandia National Laboratories is a multi-mission laboratory managed and operated by National Technology and Engineering Solutions of Sandia, LLC., a wholly owned subsidiary of Honeywell International, Inc., for the U.S. Department of Energy's National Nuclear Security Administration under contract DE-NA0003525. This work was authored [in part] by the National Renewable Energy Laboratory, operated by Alliance for Sustainable Energy, LLC, for the U.S. Department of Energy (DOE) under Contract no. DE-AC36-08GO28308. Funding provided by the U.S. Department of Energy Office of Energy Efficiency and Renewable Energy Wind Energy Technologies Office. The views expressed in the article do not necessarily represent the views of the U.S. Department of Energy or the United States Government. The U.S. Government retains and the publisher, by accepting the article for publication, acknowledges that the U.S. Government retains a nonexclusive, paid-up, irrevocable, worldwide license to publish or reproduce the published form of this work, or allow others to do so, for U.S. Government purposes.

References

Arup, Atcheson C (2016) Structural forces and stresses for wave energy devices. Technical Report ARP-LS2, Wave Energy Scotland

Babarit A, Delhommeau G (2015) Theoretical and numerical aspects of the open source BEM solver NEMOH. In: 11th European wave and tidal energy conference (EWTEC2015)

Choi J, Yoon SB (2009) Numerical simulations using momentum source wave-maker applied to RANS equation model. Coast Eng 56(10):1043–1060

Coe RG, Michelen C, Eckert-Gallup A, Martin N, Yu YH, van Rij J, Quon EW, Manuel L, Nguyen P, Esterly T, Seng B, Stuart Z, Canning J (2018a) WEC design response toolbox (WDRT). http://wec-sim.github.io/WDRT

Coe RG, Yu YH, van Rij J (2018b) A survey of WEC reliability, survival and design practices. Energies 11(1):4. https://doi.org/10.3390/en11010004, http://www.mdpi.com/1996-1073/11/1/4

Courant R, Friedrichs K, Lewy H (1928) Über die partiellen differenzengleichungen der mathematischen physik. Mathematische annalen 100(1):32–74

Crespo AJ, Domínguez JM, Rogers BD, Gómez-Gesteira M, Longshaw S, Canelas R, Vacondio R, Barreiro A, García-Feal O (2015) Dualsphysics: open-source parallel CFD solver based on smoothed particle hydrodynamics (SPH). Comput Phys Commun 187:204–216

Dallman A, Neary V (2014) Characterization of U.S. wave energy converter (WEC) test sites: a catalogue of met-ocean data. Tech. Rep. Tech. Rep. SAND2014-18206, Sandia National Laboratories

DNV-RP-C205 (2007) Environmental conditions and environmental loads. Det Norske Veritas (DNV), Høvik, Norway

DNV-RP-F205 (2010) Global performance analysis of deepwater floating structures. Det Norske Veritas (DNV), Oslo

DNV-OS-J103 (2013) Design of floating wind turbine structures. Det Norske Veritas (DNV), Høvik, Norway

Ferziger JH, Peric M (2012) Computational methods for fluid dynamics. Springer, New York

Hadzic H (2006) Development and application of finite volume method for the computation of flows around moving bodies on unstructured, overlapping grids. PhD thesis, Technische Universität Hamburg, 10.15480/882.231, https://tubdok.tub.tuhh.de/handle/11420/233

Hadzic I, Hennig J, Peric M, Xing-Kaeding Y (2005) Computation of flow-induced motion of floating bodies. Appl Math Model 29(12):1196–1210. https://doi.org/10.1016/j.apm.2005.02.014

Hérault A, Bilotta G, Dalrymple RA (2010) SPH on GPU with CUDA. J Hydraul Res 48:74–79

Hu ZZ, Causon DM, Mingham CG, Qian L (2011) Numerical simulation of floating bodies in extreme free surface waves. Nat Hazards Earth Syst Sci 11(2):519–527. https://doi.org/10.5194/nhess-11-519-2011

IEC TS 61400-3-2 (2013) Design requirements for floating offshore wind turbines, edn 2. International Electrotechnical Commission (IEC)

IEC TS 62600-2 (2016) Marine energy—Wave, tidal and other water current converters. Part 2: design requirements for marine energy systems, edn 1. International Electrotechnical Commission (IEC)

ITTC (2011) Practical guidelines for ship CFD applications. Technical Report 75-03-02-03. International Towing Tank Conference (ITTC), Rio de Janeiro, Brazil

Iturrioz A, Guanche R, Lara J, Vidal C, Losada I (2015) Validation of OpenFOAM for oscillating water column three-dimensional modeling. Ocean Engineering 107:222–236. https://doi.org/10.1016/j.oceaneng.2015.07.051, http://www.sciencedirect.com/science/article/pii/S0029801815003649

Madhi F, Yeung RW (2017) On survivability of asymmetric wave-energy converters in extreme waves. Renew Energy 119:891–909

Mundon T, Rosenberg B, Vining J (2017a) A hybrid drive train for low-speed, linear WEC applications. In: Proceedings of the 5th Marine Energy Technology Symposium (METS), Washington, D.C

Mundon TR, Rosenberg BJ, van Rij J (2017b) Reaction body hydrodynamics for a multi-DOF point-absorbing WEC. In: 12th European wave and tidal energy conference (EWTEC2017)

NORSOK (2007) Actions and action effects (N-003), edn 2. Standards Norway, Norway

Ochi MK (2005) Ocean waves: the stochastic approach, vol 6. Cambridge University Press, Cambridge

Omidvar P, Stansby PK, Rogers BD (2013) SPH for 3D floating bodies using variable mass particle distribution. Int J Numer Methods Fluids 72(4):427–452. https://doi.org/10.1002/fld.3749

OrcaFlex (2015) OrcaFlex manual. Orcina Ltd., Daltongate Ulverston Cumbria, UK

Palm J, Eskilsson C, Paredes GM, Bergdahl L (2016) Coupled mooring analysis for floating wave energy converters using CFD: formulation and validation. Int J Mar Energy 16:83–99

Penalba M, Davidson J, Windt C, Ringwood JV (2018) A high-fidelity wave-to-wire simulation platform for wave energy converters: coupled numerical wave tank and power take-off models. Appl Energy 226:655–669

Quon E, Platt A, Yu YH, Lawson M (2016) Application of most likely extreme response method for wave energy converters. In: ASME 2016 35th international conference on ocean, offshore and arctic engineering (OMAE), ASME

Rafiee A, Wolgamot H, Draper S, Orszaghova J, Fivez J, Sawyer T(2016) Identifying the design wave group for the extreme response of a point absorber wave energy converter. In: Asian wave and TidalEnergy conference (AWTEC), Singapore

Ransley E, Greaves D, Raby A, Simmonds D, Hann M (2017a) Survivability of wave energy converters using CFD. Renew Energy 109:235–247

Ransley E, Greaves D, Raby A, Simmonds D, Jakobsen MM, Kramer M (2017b) RANS-VOF modelling of the wavestar point absorber. Renew Energy 109:49–65

Rosenberg B, Mundon T (2016) Numerical and physical modeling of a flexibly-connected two-body wave energy converter. In: Proceedings of the 4th marine energy technology symposium (METS), Washington, D.C.

Schetz J (1993) Boundary layer analysis. Prentice Hall, https://books.google.com/books?id=vcNvQgAACAAJ

Sjökvist L, Göteman M (2017) Peak forces on wave energy linear generators in tsunami and extreme waves. Energies 10(9):1323

van Rij J, Yu YH, Coe RG (2018) Design load analysis for wave energy converters. In: ASME 2018 37th international conference on ocean, offshore and arctic engineering (OMAE2018), ASME, Madrid, Spain

Vinokur M (1983) On one-dimensional stretching functions for finite-difference calculations. J Comput Phys 50(2):215–234

Westphalen J, Greaves D, Williams C, Taylor P, Causon D, Mingham C, Hu Z, Stansby P, Rogers B, Omidvar P (2009) Extreme wave loading on offshore wave energy devices using CFD: a hierarchical team approach. In: Proceedings of the 8th European wave and tidal energy conference (EWTEC), pp 500–508

Westphalen J, Greaves MD, Raby A, Hu ZZ, Causon DM, Mingham CG, Omidvar P, Stansby PK, Rogers BD (2014) Investigation of wave-structure interaction using state of the art CFD techniques. Open J Fluid Dyn 04(01):18–43. https://doi.org/10.4236/ojfd.2014.41003

Yu YH, Li Y (2013) Reynolds-averaged Navier-Stokes simulation of the heave performance of a two-body floating-point absorber wave energy system. Comput Fluids 73:104–114. https://doi.org/10.1016/j.compfluid.2012.10.007